Interferometric fluorescent super-resolution microscopy resolves 3D cellular ultrastructure

Gleb Shtengel[a], James A. Galbraith[b], Catherine G. Galbraith[c], Jennifer Lippincott-Schwartz[d,1], Jennifer M. Gillette[d], Suliana Manley[d], Rachid Sougrat[d], Clare M. Waterman[e], Pakorn Kanchanawong[e], Michael W. Davidson[f], Richard D. Fetter[a], and Harald F. Hess[a,1]

[a]Howard Hughes Medical Institute, Janelia Farm Research Campus, Ashburn, VA 20147; [b]National Institute of Neurological Disorders and Stroke; [c]National Institute of Dental and Craniofacial Research; [d]Cell Biology and Metabolism Branch, National Institute of Child Health and Human Development; and [e]Laboratory of Cell and Tissue Morphodynamics, National Heart Lung and Blood Institute, National Institutes of Health, Bethesda, MD 20892; and [f]National High Magnetic Field Laboratory and Department of Biological Sciences, Florida State University, Tallahassee, FL 32310

Understanding molecular-scale architecture of cells requires determination of 3D locations of specific proteins with accuracy matching their nanometer-length scale. Existing electron and light microscopy techniques are limited either in molecular specificity or resolution. Here, we introduce interferometric photoactivated localization microscopy (iPALM), the combination of photoactivated localization microscopy with single-photon, simultaneous multiphase interferometry that provides sub-20-nm 3D protein localization with optimal molecular specificity. We demonstrate measurement of the 25-nm microtubule diameter, resolve the dorsal and ventral plasma membranes, and visualize the arrangement of integrin receptors within endoplasmic reticulum and adhesion complexes, 3D protein organization previously resolved only by electron microscopy. iPALM thus closes the gap between electron tomography and light microscopy, enabling both molecular specification and resolution of cellular nanoarchitecture.

fluorescence microscopy | interferometry | PALM | photoactivated localization microscopy | single molecule imaging

A fundamental question in biomedical research is how specific, nanometer-scale biomolecules are organized into multicomponent micron-scale structural and signaling ensembles that facilitate cell function. For example, microtubules are built of 8-nm tubulin subunits that incorporate on the ultrastructural level into polymers 25 nm in diameter and >10 μm in length that serve as the building blocks of superstructures such as mitotic spindles and flagella. However, key challenges remain for determining cellular ultrastructure with high molecular specificity. Because cellular structures are organized on the nanoscale, nanometer resolution is required. Immunoelectron microscopy (EM)-based approaches provide the necessary resolution, but they lack robust molecular specificity because the large size of the antibodies hampers their penetration into dense structures and the specificity of the antibody can be compromised by cross-reactivity and epitope masking caused by the harsh fixation often used for high-resolution EM. Fluorescence microscopy coupled with fluorescent protein (FP) fusion technology enables imaging cellular structure with exquisite molecular specificity, but the resolution of 3D images is diffraction-limited to ≈200 nm in the lateral and ≈500 nm in the axial direction, limiting conventional fluorescence to the characterization of cellular superstructure. Some of the recent fluorescence-based super-resolution microscopy techniques (1–5) demonstrated a resolution of <100 nm in the vertical direction; however, this is still insufficient to bridge the resolution gap between cellular ultrastructure and superstructure. To achieve near-ultrastructural 3D resolution even for the limited photon outputs of high-molecular-specificity FPs, we have developed a single-photon multiphase interferometric scheme and integrated it with a lateral photoactivated localization microscopy (PALM) (6),

resulting in a highly photon-efficient system called interferometric PALM (iPALM).

Quantitative high-precision positional measurements are commonly made with phase-based interferometry (7), where coherent light waves from 2 optical paths (a reference path and a measured path) are combined to create a signal that modulates on the length scale of an optical wavelength. Interferometry is widely applied to position objects to 10^{-10}-meter accuracy, measure optical surfaces, and even scout for gravity waves with 10^{-18}-meter sensitivity. Interferometric microscopes (8, 9) when combined with phase-shifting techniques (10) can form sub-nanometer-height images and are routinely used in industry to qualify semiconductor processing or hard disk drive head profiles. However, the benefit of such a quantitative interferometric method has so far been elusive for biological systems, despite the wealth of open questions that hinge on the 3D molecular organization at the nanometer scale. Most biological imaging applications use Nomarski differential interference contrast, Zernike phase contrast, or interference reflection microscopy, which harness qualitative interferometric contrast that depends on the refractive index variations within biological materials and forgoes the molecular specificity afforded by fluorescent labeling. Other more recent concepts, such as 4π (11) and I^{5}M (12), use interference to create a more precise vertical focus (point-spread function) but do not extract explicit phase values from the interfered signal, a critical advantage that is exploited by phase-shifting techniques. One quantitative approach (13) measures the phase of a fluorescent source but requires multiple replicas of the same sample structure over a patterned silicon substrate, a very limiting requirement for bioimaging.

The obstacles to the precise measurement of biological samples by phase-shifting interferometry techniques may seem fundamental. Cells, tissues, or other biological materials typically lack single well-defined reflecting surfaces and interact with visible light weakly and with low molecular specificity. On the other hand, fluorescence provides superb molecular specificity but poses a new problem for interferometry: how to form 2 path-dependent phase coherent beams that can undergo interference. The brightness of fluorescent labels is also highly variable because of photobleaching and other photophysical
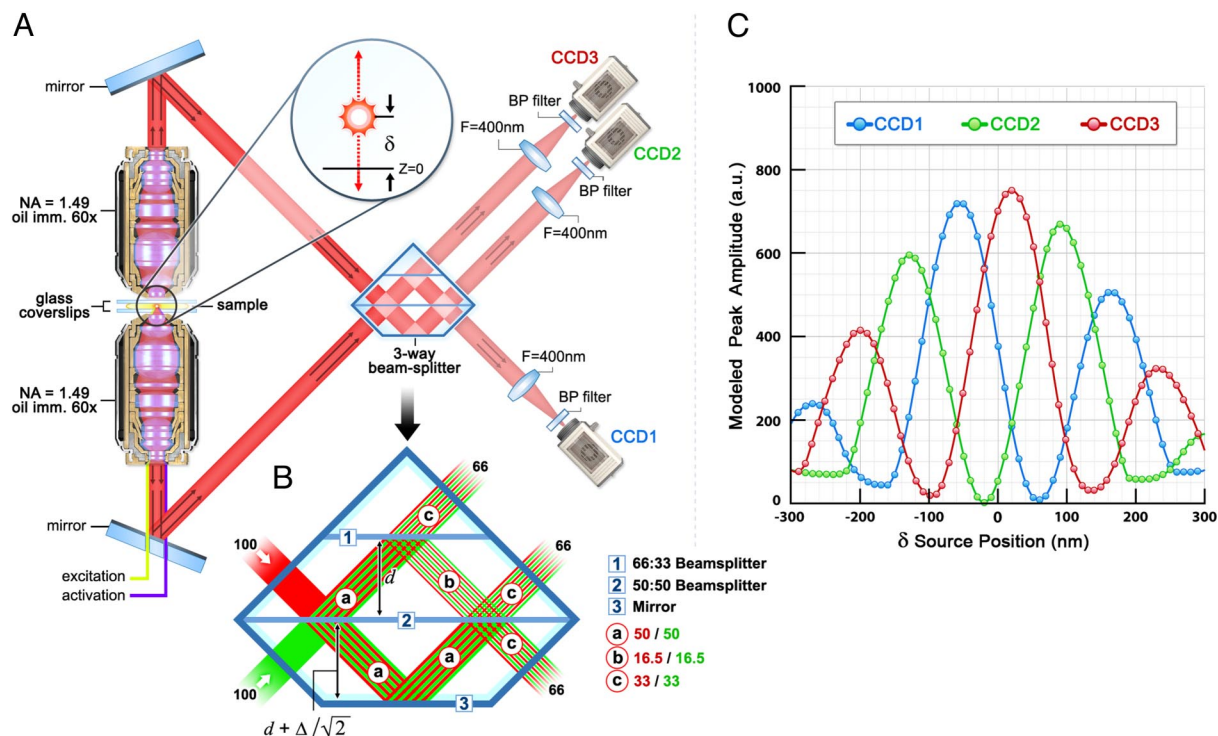
Fig. 1. Schematics and operating principle of multiphase interferometric microscope illustrating how Z-position is resolved. (*A* and *B*) Schematic of the single-photon multiphase fluorescence interferometer. A point source with z-position δ emits a single photon both upwards and downwards. These 2 beams (color coded as red and green in *B*) interfere in a special 3-way beam splitter. (*C*) The self-interfered photon propagates to the 3 color-coded CCD cameras with amplitudes that oscillate 120° out of phase as indicated.

processes, factors that undermine the ability to take multiple sequential measurements and reliable calibrations that form the basis of phase-shift interferometry.

We have configured an optical system to overcome these obstacles using a combination of insights. First, single fluorescent molecules such as FPs are intrinsic quantum sources. Thus, wave-particle duality allows a single fluorescent photon to form its own coherent reference beam. An emitted photon can simultaneously travel 2 distinct optical paths, which are subsequently recombined so that the photon interferes with itself. The position of the emitter directly determines the difference in the path lengths, hence the relative phase between the 2 beams. This principle has been used in fluorescence interferometry (13, 14) and spectral self-interference fluorescence microscopy (15). Second, the optical system can be configured so that interference can take place over a wide range of lateral source positions to form interference images on an area array detector, such as a CCD for rapid parallel acquisition. Finally and most importantly, *simultaneous multiphase* detection must be implemented for each photon. Such detection methodology is tolerant to intensity variations and short fluorescent lifetimes; it ensures proper self-calibration, and provides complete information to extract a position-dependent interference phase angle.

Results and Discussion

The essence of the single-photon interferometric fluorescence imaging concept is illustrated in Fig. 1, and core to this concept is a custom 3-way beam splitter. Three-way or even higher-order beam splitters are commonly used in a single-mode context (16–18) such as fiber optic gyroscopes, planar waveguide devices for telecommunications, or precision metrology of an object's position. Our device extends this multiphase interference beyond the single-mode, single-point case to the multiphase, and multiple-source case necessary for imaging biological samples. It is composed of 3

parallel planes of a 66:33 beam splitter, a 50:50 beam splitter, and a mirror (Fig. 1*B*). Self-interference of a single-photon source (such as a fluorescent protein in a sample) placed at the focal plane of 2 opposed objectives enables a precise determination of its axial position. Upon radiation, a fluorescent photon simultaneously enters both the upper and lower objectives, as illustrated in Fig. 1*A*. The difference in path lengths of the upper and lower beams directly depends on the axial position of the source. Because the photon self-interferes in the 3-way beam splitter, this position-dependent phase difference modulates the relative intensities of the 3 output beams as shown in Fig. 1*C*. Therefore, the axial position of the source molecule can be determined from the relative amplitudes of the source images from the 3 cameras. Localized lateral positions of a source molecule can be extracted by finding their centers from the same image set so that no extra data acquisition is needed to obtain the full 3D data coordinates. The mathematical description is presented below. The experimental validation of the performance of iPALM, as well as a tutorial demonstrating the interferometry concept are presented in [supporting information (SI)](#).

The resolution capability of iPALM for determining the 3D location on the length scale of biomolecules is presented in Fig. 2. The localization accuracy of a single fluorescent source imaged repetitively for 25,000 frames is shown in Fig. 2*A*. Even with only 1,500 photons into a 4π solid angle (1,200 photons detected), iPALM resolves the position of the source with full width at half maximum (FWHM) of 9.8 nm axially. The lateral position is derived from the centroid of the image spot (19) and the lateral localization accuracy of this same source has FWHM of 22.8 nm. Fig. 2*B* compares the dependence of localization accuracy on source brightness for iPALM compared with superresoultion defocusing approaches (2, 3, 20, 21). Localization accuracy depends critically on source brightness, and scales approximately as the inverse square root of the number of photons detected. This
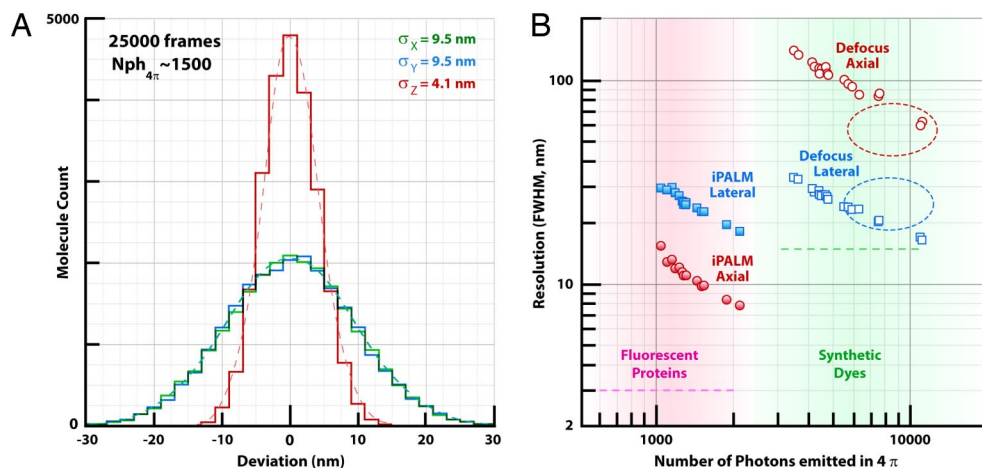
Fig. 2. X, Y, Z resolution of iPALM and its dependence on source brightness, illustrating iPALM's sub-20-nm 3D resolution with endogenous FP labels. (*A*) A histogram of experimentally determined positions from repeatedly sampling (25,000 frames) a source where ≈1,200 photons are detected per frame from ≈1,500 photons emitted into a 4π solid angle. (*B*) Axial (solid red circles) and lateral (solid blue squares) resolution of iPALM determined from FWHM of localization of Au beads of different brightness. Note that the positional FWHM number is 2.4 times larger than σ the variance that is also used to characterize resolution. Axial (empty red circles) and lateral (empty blue squares) resolution of the defocusing method determined from FWHM of localized position of Au beads of different brightness. Large ovals indicate approximately the published results for axial (red) and lateral (blue) resolutions of 3D STORM (2) and BP PALM (3). The typical photon output of fluorescent protein tags and synthetic fluorophores are depicted as pink and green gradients. Also shown (horizontal dashed lines) are addition uncertainties resulting from the displacement between the target protein and the fluorescent probes for different imaging methods.

illustrates that iPALM provides 10-fold improvement in axial resolution and 100-fold improvement in photon efficiency compared with the defocus-based techniques (Fig. 2*B*). Thus, where defocusing methods require antibody-based or cytochemical methods for labeling proteins with brighter organic fluorochromes, iPALM allows accurate localization of FPs even with their modest photon output (typically 500 detected photons for a 2π solid angle). In addition to the advantages of a genetically encoded fluorescent label for specificity, the small size of FPs (3–4 nm) compared with antibodies (>10 nm) confers improvements in spatial sampling density and significantly reduces the localization uncertainty because of probe size, which, in the case of antibody, can introduce up to 15 nm in additional FWHM. These additional uncertainties are illustrated by dotted lines in Fig. 2*B*. An additional benefit of iPALM compared with defocus-based methods is a factor of 2 better lateral resolution because of the factor of 2 (dual objectives) better photon collection efficiency and the optimal image focusing (2, 3).

We demonstrate the 3D superresolution capability of iPALM on fixed cells expressing photoswitchable or photoactivatible FP fusion proteins. The multiphase interferometric microscopy (the *i* in iPALM) recovers the *z*–axis position, and simultaneously PALM (6, 22, 23) recovers the *x*–*y* coordinates on high densities of FP-fusion molecules that occur in cellular structures. Typically, >20,000 frame triplets of individually imaged photoactivatibly FPs are acquired, which capture different proteins with 10–100 labeled molecules per frame. In this manner, a compiled list of 100,000–2,000,000 molecular locations can be combined to form the basis for a 3D volume rendering of protein distributions. iPALM thereby achieves 3D protein-specific contrast images at the size scale associated with electron tomography.

To demonstrate the resolution and sensitivity of iPALM, we imaged well-characterized cellular ultrastructure. Electron microscopy has established that microtubules, which serve as a polarized structural scaffold within cells, have a 25 nm diameter (24). Previous fluorescent-based superresolution 3D imaging approaches (2–4) have lacked the resolution to demonstrate this size. With iPALM, we have resolved the diameter of the microtubules to nearly their known dimension along the *z* axis. This is illustrated in the iPALM image Fig. 3 of a PtK1 cell expressing human α-tubulin

fused to a monomeric variant of the fluorescent protein KikGR (25). The color-coded height image of multiple microtubules crossing each other vertically shows individual microtubules as distinct colors (Fig. 3*C*). A *z* axis histogram (Fig. 3*D*) for 2 of the microtubules crossing within 70 nm of each other (boxed region in Fig. 3*A*) shows a FWHM of 25–30 nm for each microtubule. This size is in good agreement with the dimension of the microtubule itself plus the size of the FP (24). This illustrates the power of iPALM to reveal the 3D morphology with high molecular specificity on a scale
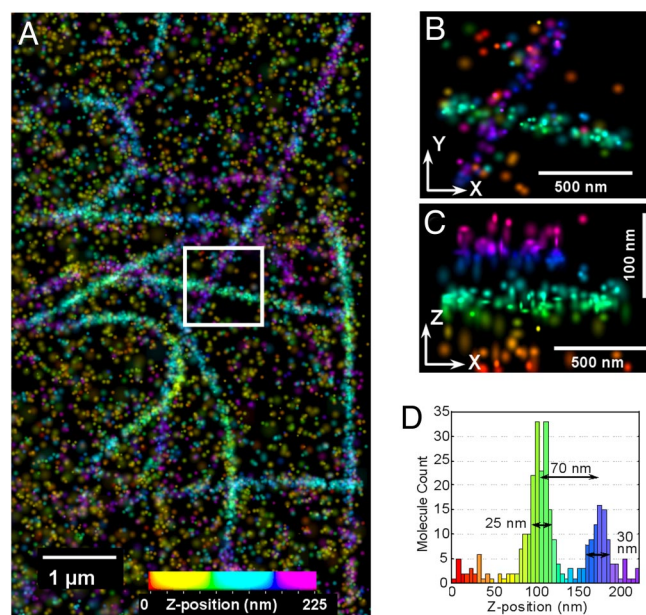
Fig. 3. Superresolution iPALM image of microtubules in a PtK1 cell expressing human α-tubulin fused to *m*-KikGR, rendered with *z* axis color-coding. (*A*) Large area overview. (*B* and *C*) Zoom-in of the area bound by the white box in *X*–*Y* (*B*) and *Z*–*Y* (*C*) projections (*z*-scale is magnified 5×). (*D*) Histogram of *z*-positions of molecules in the boxed region. Each microtubule has a FWHM of 30 nm, and the separation distance of 70 nm between the cyan and purple microtubules is easily resolved.
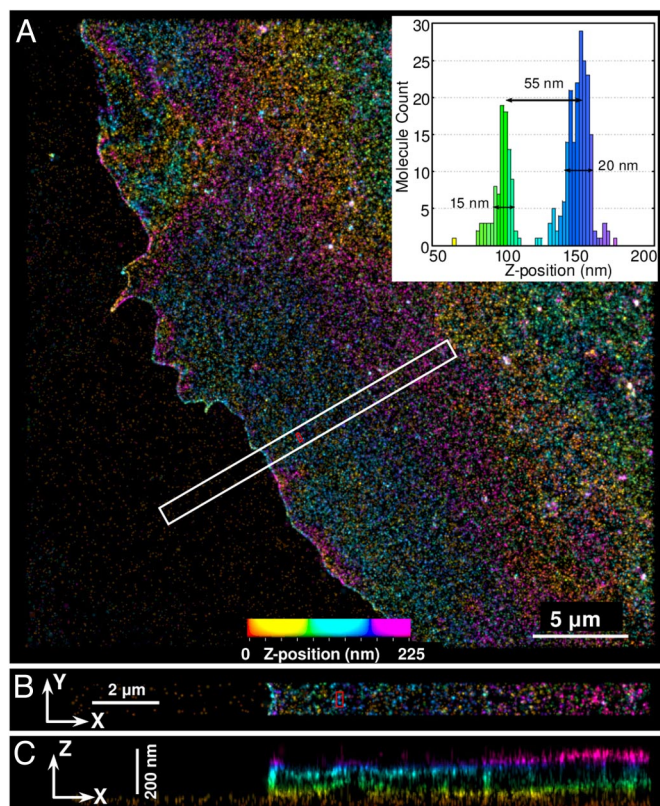
Fig. 4. Superresolution iPALM image of COS7 cell expressing the membrane protein VSVG fused to td-EosFP, rendered with z axis color-coding. (*A*) Large area overview. (*B* and *C*) Area outlined in white is enlarged in *B* and shown in *C* as a z cross-section. Shown in the *Inset* is the histogram of vertical distribution of fluorescent molecules in the area limited by the red rectangle.

Fig. 5. U2OS cell expressing td-EosFP-α_v-integrin. (*A–C*) Widefield (*A*) and PALM (*B*) images, and z color-coded iPALM image (*C*). The coverslip surface (CS), focal adhesion (FA), cell plasma membrane (PM), and endoplasmic reticulum (ER) can be identified. (*D*) Z-position histogram of area limited by the green box in *C* with peaks corresponding to CS and FA. (*E* and *F*) X–Y (*E*) and X–Z (*F*) projections of the area bound by the white box in *C*. Z-scale is magnified by 4 in *F*.

relevant for understanding how these proteins are organized and function with other molecular partners within the cell.

Another class of biological structures where iPALM can provide insights is the plasma membrane system, which serves as the boundary between the cytoplasm and extracellular environment. To visualize the plasma membrane, COS-7 cells were transiently transfected with the transmembrane vesicular stomatitis virus G protein (VSVG) tagged with tandem-dimer-Eos FP (tdEosFP) (26). The vertical position of VSVG molecules in the plasma membrane over a 225-nm range is represented by a color hue scale (Fig. 4). A cross-section of the area bound by the white rectangle separately resolves both the dorsal and ventral plasma membrane, even for spacings ≈60 nm and shows a cell surface protrusion with an average thickness of 110–160 nm (Fig. 4*C*), consistent with electron microscopy (27). The lateral dimensions of the displayed area are an order of magnitude wider than the vertical scale so the vertical variations because of membrane roughness manifest as increased apparent membrane thickness in the cross-section. Atomic force microscopy (AFM) measures membrane roughness with the same degree of precision (28), however, with iPALM, we are able to access the topology of the membrane opposing the coverslip with equal precision, which AFM cannot. With the axial resolution provided by iPALM, issues such as plasma membrane polarity and endocytic protein organization can now be investigated at the molecular level.

The molecular precision and spatial resolution of iPALM are especially useful for probing the endomembrane system and its interaction with other cellular structures, particularly in the axial dimension. The 3D mapping of another membrane protein, α_v integrin fused with tdEos, coexpressed with untagged β_1 integrin

in U2OS cells, demonstrates this capability (Fig. 5). Integrins are $\alpha\beta$ heterodimeric transplasma-membrane receptors that cluster in the membrane to form focal adhesions (FAs), where they bind to the extra extracellular matrix and serve as mechanical and signaling linkages between the cells and their environment. The iPALM image (Fig. 5*C*) with color-encoded vertical position clearly identify those integrin α_v molecules that are incorporated into FAs (yellow in Fig. 5 *C*, *E*, and *F*), whereas a sparser distribution of α_v integrins outline the contour of the plasma membrane. Furthermore, a network of tubular structures is observed at >70 nm above the coverslip plane, which reveals the endoplasmic reticulum (ER) decorated by newly synthesized α_v integrin. The iPALM image clearly identifies finger-like ER structures juxtaposing FA, suggestive of their involvement in integrin delivery (see SI for a movie clearly resolving the ER lumen). Within an FA, α_v integrin occupies a very narrow height distribution of <15-nm FWHM at a vertical displacement of ≈35 nm above the coverslip surface, in good agreement with the cell–substratum separation of ≈15–20 nm, known from electron or interference reflection microscopy (27, 29). Together with the plasma membrane thickness and the position of the tdEos FP tag at the cytoplasmic domain of the integrin α_v, it is also in agreement with the distance between integrin-based adhesions and coverglass determined by interference reflection microscopy (29). The demonstrated 15-nm precision (FWHM) of vertical localization of FP-tagged integrin illustrates the poten-

tial for iPALM for determining the structural basis of the link between the extracellular matrix and cell cytoskeleton via the various proteins within focal adhesions.

In summary, we have described an iPALM imaging system that achieves sub-20-nm 3D spatial resolution and demonstrated its imaging capability with photoactivatable FPs. Having thus overcome the brightness limitation of FPs, iPALM can take full advantage of their intrinsic biological compatibility, specificity, and versatility. We have shown that iPALM can clearly resolve microtubules and adhesion complexes close to their known dimensions, and thus provides sufficient resolving power for probing protein organizations within molecular assemblies in the cells. Application of iPALM with optically distinct labeling of proteins should further aid in the deciphering of the molecular-scale architectures and interactions that constitute biological structures. The interferometry approach presented here can also be directly applied to single-particle tracking (30) to study 3D protein trafficking and diffusion through the cytosol, on membranes, or transport properties along cytoskeletal scaffolds. The examples of 3D superresolution imaging we present here reveal the power of iPALM for the quantitative measurement of protein distribution and topology in biological structures at the nanoscale, heralding future dynamic imaging of the molecularly specific protein nanoorganization in all organelles as they reorganize during regulation and disease.

Theoretical Foundation for iPALM. A sample, with refractive index n, comprising a single quantum source is placed at the focal planes of 2 opposed objectives. Upon radiation, a single photon of wavelength λ simultaneously enters both the upper *and* the lower objective. The 2 beams have the path-dependent electric fields $E_0 \exp(ik\delta)$ and $E_0 \exp(-ik\delta)$, where δ is the displacement of the source from the position $z = 0$ along the z axis, omitting the common phase factor $k \approx 2\pi n/\lambda(1 + NA/8)$, the propagation factor, and n the refractive index of the sample medium. The factor $(1 + NA/8)$ is due to the phase anomaly in the focal region (31, 32). These 2 beams interfere in the custom 3-way beam splitter (shown in Fig. 1*B*), which is a critical part of iPALM system. Other simultaneous multiphase detection schemes have been developed and commercialized but require polarized light (33).

Assuming no optical loss in this 3-way beam splitter, the surface reflectivities as indicated in Fig. 1*B*, and $\pi/2$ phase retardation of reflected waves relative to the transmitted waves at 33% and 50% interfaces (34), we then arrive at:

$$I_1 = \frac{2}{3}I_0(1 + \sin(2k\delta))$$

$$I_2 = \frac{2}{3}I_0\left[1 - \left(\frac{1}{2}\sin(2k\delta) + \frac{\sqrt{3}}{2}\cos(2k\delta)\sin(2k\Delta)\right)\right]$$

$$I_3 = \frac{2}{3}I_0\left[1 - \left(\frac{1}{2}\sin(2k\delta) - \frac{\sqrt{3}}{2}\cos(2k\delta)\sin(2k\Delta)\right)\right],$$

[1]

where Δ is defined in Fig. 1*B*. Clearly, $I_1 + I_2 + I_3 = 2\vec{E}_0 \cdot \vec{E}_0 = 2I_0$, as expected. Furthermore, if $\sin(2k\Delta) = \pm 1$, then we can simplify Eq. **1** to:

$$I_1 = \frac{2}{3}I_0\left(1 + \sin\left(\frac{4\pi n\delta}{\lambda(1 + NA/8)}\right)\right)$$

$$I_2 = \frac{2}{3}I_0\left(1 + \sin\left(\frac{4\pi n\delta}{\lambda(1 + NA/8)} \mp \frac{2\pi}{3}\right)\right)$$

[2]

$$I_3 = \frac{2}{3}I_0\left(1 + \sin\left(\frac{4\pi n\delta}{\lambda(1 + NA/8)} \pm \frac{2\pi}{3}\right)\right)$$

The intensity of a point source varies with displacement δ according to Eq. **2** multiplied by an envelope given by the focal range (Fig. 1*C*), provided that the above split ratios hold across the wavelength range of detected signal and for all polarizations. The photon intensity cycles from detector 1 to 2 to 3 over a range of $\approx$225 nm (for $\lambda = 590$ nm, $NA = 1.4$, and $n \approx 1.4$) and any intermediate position δ along the z axis can be obtained from the formulae in the ideal case:

$$D = I_1 + I_2\exp\left(i\frac{2\pi}{3}\right) + I_3\exp\left(i\frac{4\pi}{3}\right)$$

$$\delta = \frac{\lambda(1 + NA/8)}{4\pi n}\arctan\left(\frac{D - D^*}{D + D^*}\right),$$

[3]

or deduced from calibration data to incorporate an empirical parameterization.

This multiphase interference technique has 2 critical advantages over a standard 2-way beam splitter: (*i*) twice the range of unique phase inversion and (*ii*) a relatively constant z axis position sensitivity for the composite data. By contrast, a simple 2-way beam splitter has an interference phase angle of 180° between outputs, causing the sensitivity to vanish at the intensity maximum and minimum. Such an effect leads to dead zones, reducing the measurement range of standard 2-way beam-splitter to effectively a factor of 3 smaller than that of the 3-way beam splitter.

An example of the 3 interference images of sparsely distributed fluorescent fiducials (100-nm Au particles) at a specific z height is shown in SI. The z positions derived from the intensities for all fiducials imaged over a range of displacements are shown in SI and demonstrates uniform sensitivity.

The single-molecule localization accuracy of the conventional 2D PALM system is given by the formula (19):

$$\langle\sigma^2\rangle = \frac{s^2 + a^2/12}{N} + \frac{8\pi s^4 b^2}{a^2 N^2},$$

[4]

where s is the standard deviation of the point-spread function (PSF), and N the number of photons collected, a the finite pixel size ($s > a$), and b the background noise.

The first term represents the statistical formula for the error of the mean, the second term is due to the pixelation noise, and the third term represents the uncertainty arising from the background noise.

The fundamental localization limit is represented by the first term s^2/N. In the lateral plane (x–y plane), the PSF in the image space is represented by an Airy function (35), and the standard deviation of the PSF in the lateral plane of the object space is given by:

$$s_{Airy.obj} \approx \frac{0.75 \cdot \lambda}{\pi NA}.$$

[5]

To evaluate the fundamental localization limit in z direction, we start with criterion for least-squares fitting in extracting the vertical coordinate z from the amplitudes of the signal in 3 cameras (following the same logic as ref. 19):

$$\chi^2(z) = \sum_{i=1}^{3}\frac{(A_i - N_i(z))^2}{\sigma_i^2},$$

[6]

where A_i is the signal amplitude (in number of photons) of the signal measured on camera i, N_i the expected signal amplitude on the ith camera for vertical coordinate z (defined by Eq. **2**), and σ_i the expected uncertainty given by the sum of the uncertainties due to photon counting noise and background noise. Following

the derivations in ref. 19, we obtain the expression for the standard deviation of localization along z axis:

$$\sigma_{z-iPALM} = \frac{s_{z-iPALM}}{\sqrt{N_{tot}}}, \text{ where } s_{z-iPALM} = \frac{\lambda(1 + NA/8)}{4\pi n}.$$

[7]

For aqueous sample medium with $n \approx 1.33$, $\lambda = 590$ nm, and for $NA = 1.4$, Eqs. **5** and **7** give the localization accuracies of $\sigma_{x,y} \approx 100$ nm/$\sqrt{N_{tot}}$ and $\sigma_z \approx 40$ nm/$\sqrt{N_{tot}}$.

It should be pointed out that the only approximation made in deriving Eq. **7** is the omission of the background noise, so when compared with localization accuracy in x–y plane it should be compared with the first 2 terms in Eq. **4**.

The contribution of the background noise (third term in Eq. **4**) scales as s^4, so its relative contribution is smaller for z axis localization then that x–y-plane localization.

Biological samples do have index variations that can give additional phase shifts to the radiating photons that depend on direction and the optical index along that path. This gives rise to slowly varying (over micron lateral scale) distortions. For example the position of molecules on the coverslip surface appear not flat but bowed down by 2–5 nm under a cell of Fig. 4 or Fig. 5. This results from a higher index cell in a lower index aqueous media. However, a reference plane such as fluorescent layer localized on a glass surface allows one to monitor the error from index changes and offers a reference by which to correct for it.

The details of experimental setup and sample preparation are given in SI.

1. Gustafsson MGL, *et al.* (2008) Three-dimensional resolution doubling in wide-field fluorescence microscopy by structured illumination. *Biophys J* 94(12):4957–4970.
2. Huang B, Wang WQ, Bates M, Zhuang XW (2008) Three-dimensional super-resolution imaging by stochastic optical reconstruction microscopy. *Science* 319(5864):810–813.
3. Juette MF, *et al.* (2008) Three-dimensional sub-100 nm resolution fluorescence microscopy of thick samples. *Nat Methods* 5(6):527–529.
4. Schmidt R, *et al.* (2008) Spherical nanosized focal spot unravels the interior of cells. *Nat Methods* 5(6):539–544.
5. Vaziri A, Tang J, Shroff H, Shank CV (2008) Multilayer 3-dimensional super resolution imaging of thick biological samples. *Proc Natl Acad Sci USA* 105(51):20221–20226.
6. Betzig E, *et al.* (2006) Imaging intracellular fluorescent proteins at nanometer resolution. *Science* 313(5793):1642–1645.
7. Hariharan P (2003) *Optical Interferometry* (Academic, Boston), 2nd Ed, p 351.
8. Linnik VP (1933) Simple interferometer for the investigation of optical systems. *C R Acad Sci* 1:208–210.
9. Delaunay G (1953) Microscope interférentiel A. Mirau pour la mesure du fini des surfaces. *Rev Opt Theor Instrum* 32:610–614.
10. Bhushan B, Wyant JC, Koliopoulos CL (1985) Measurement of surface-topography of magnetic tapes by mirau interferometry. *Appl Opt* 24(10):1489–1497.
11. Hell S, Stelzer EHK (1992) Fundamental improvement of resolution with a 4pi-confocal fluorescence microscope using 2-photon excitation. *Opt Commun* 93(5–6):277–282.
12. Gustafsson MGL, Agard DA, Sedat JW (1995) Sevenfold improvement of axial resolution in 3D widefield microscopy using two objective lenses. *Proc SPIE* 2412:147–156.
13. Braun D, Fromherz P (1998) Fluorescence interferometry of neuronal cell adhesion on microstructured silicon. *Phys Rev Lett* 81(23):5241–5244.
14. Bilenca A, *et al.* (2008) Fluorescence interferometry—Principles and applications in biology. *Fluor Methods Appl Spectr Imaging Probes* 1130:68–77.
15. Dogan M, *et al.* (2008) Spectral self-interference fluorescence microscopy for subcellular imaging. *IEEE J Sel Top Quant Electron* 14(1):217–225.
16. Poisel H, Trommer G (1990) Optical-fiber gyroscope of sagnac type having a fiber-optic loop and 3×3 coupler. *US Patent* 4,944,590.
17. Peale D, Duran C, Hess H (2004) Waveguide based parallel multi-phaseshift interferometry for high speed metrology, optical inspection, and non-contact sensing. *US Patent* 6,687,008.
18. Peale DR, Hess H (2008) Evanescent waveguide couplers. *US Patent* 7,333,690.
19. Thompson RE, Larson DR, Webb WW (2002) Precise nanometer localization analysis for individual fluorescent probes. *Biophys J* 82(5):2775–2783.
20. van Oijen AM, Köhler J, Schmidt J, Müller M, Brakenhoff (1998) GJ 3-Dimensional super-resolution by spectrally selective imaging *Chem Phys Lett* 292(1–2):183–187.
21. Pin Kao H, Verkman AS (1994) Tracking of single fluorescent particles in three dimensions: Use of cylindrical optics to encode particle position. *Biophys J* 67(3):1291–1300.
22. Hess ST, Girirajan TPK, Mason MD (2006) Ultra-high resolution imaging by fluorescence photoactivation localization microscopy. *Biophys J* 91(11):4258–4272.
23. Rust MJ, Bates M, Zhuang X (2006) Sub-diffraction-limit imaging by stochastic optical reconstruction microscopy (STORM). *Nat Methods* 3(10):793–796.
24. Osborn M, Webster RE, Weber K (1978) Individual microtubules viewed by immunofluorescence and electron-microscopy in same Ptk2 cell. *J Cell Biol* 77(3):R27–R34.
25. Habuchi S, Tsutsui H, Kochaniak, AB, Miyawaki A, van Oijen AM (2009) mKikGR, a monomeric photoswitchable fluorescent protein. *PLoS ONE* 3(12).
26. Wiedenmann J, *et al.* (2004) EosFP, a fluorescent marker protein with UV-inducible green-to-red fluorescence conversion. *Proc Natl Acad Sci USA* 101(45):15905–15910.
27. Abercrombie M, Heaysman JE, Pegrum SM (1971) The locomotion of fibroblasts in culture. IV. Electron microscopy of the leading lamella. *Exp Cell Res* 67(2):359–367.
28. Frankel DJ, *et al.* (2006) Revealing the topography of cellular membrane domains by combined atomic force microscopy/fluorescence imaging. *Biophys J* 90(7):2404–2413.
29. Izzard CS, Lochner LR (1976) Cell-to-substrate contacts in living fibroblasts—Interference reflection study with an evaluation of technique. *J Cell Sci* 21(1):129–159.
30. Manley S, *et al.* (2008) High-density mapping of single-molecule trajectories with photoactivated localization microscopy. *Nat Methods* 5(2):155–157.
31. Gouy LG (1890) Sur une propriete nouvelle des ondes lumineuses. *C R Acad Sci* 110:1251–1253.
32. Linfoot EH, Wolf E (1956) Phase distribution near focus in an aberration-free diffraction image. *Proc Phys Soc B* 69:823–832.
33. Millerd JE, Brock NJ (2001) Methods and apparatus for splitting, imaging, and measuring wavefronts in interferometry *US Patent* 6,304,330.
34. Hecht E (1998) *Optics* (Addison—Wesley, Reading, MA), 3rd Ed, Section 9.6.
35. Born M, Wolf E (1984) *Principles of Optics* (Pergamon, Oxford), 6th Ed, Section 8.5.2.